

Robustness of type-II Dirac cones in biphenylene: From nanoribbons to symmetric bilayer stackingL. L. Lage ¹, O. Arroyo-Gascón ^{2,3,*}, Leonor Chico ³ and A. Latgé ¹¹*Instituto de Física, Universidade Federal Fluminense, Niterói, Avenida Litorânea sn 24210-340, Rio de Janeiro, Brazil*²*Instituto de Ciencia de Materiales de Madrid, Consejo Superior de Investigaciones Científicas,**C/Sor Juana Inés de la Cruz 3, 28049 Madrid, Spain*³*GISC, Departamento de Física de Materiales, Facultad de Ciencias Físicas, Universidad Complutense de Madrid, E-28040 Madrid, Spain*

(Received 17 July 2024; revised 13 September 2024; accepted 2 October 2024; published 17 October 2024)

The electronic properties of one- and two-dimensional biphenylene-based systems, such as nanoribbons and bilayers, are studied within a unified approach. Besides the bilayer with direct (AA) stacking, we found two additional symmetric stackings for bilayer biphenylene that we denote by AB, in analogy with bilayer graphene, and AX, which can be derived by a small translation (slip) from the AA bilayer, with distinct electronic band structures. We combine first-principles calculations with a long-range tight-binding model to provide a realistic effective description of these biphenylene materials. Our approach provides a global framework to analyze realistically the robustness of the characteristic type-II Dirac cones present in all the bilayers studied and of the nanoribbons. In particular, we capture the opening in the Dirac cone for certain nanoribbons, which we relate to the symmetries of the system, as well as the variations caused by different stackings. We expect that these structures will constitute an avenue to explore novel physics, as they occur with bilayer graphene and the one-dimensional derivatives of graphene, such as nanoribbons and nanotubes.

DOI: [10.1103/PhysRevB.110.165423](https://doi.org/10.1103/PhysRevB.110.165423)**I. INTRODUCTION**

Carbon-based two-dimensional (2D) crystals, particularly those structured with hexagonal (benzene) rings, have garnered significant interest beyond graphene systems. These new allotropes include monolayer structures such as those synthesized in recent studies [1], bilayer structures [2,3], and graphdiyne [4], which is characterized by the insertion of *sp* acetylenic bonds within the carbon lattice. Other carbon materials without hexagonal carbon rings have been theoretically proposed, such as pentaheptite [5], completely composed of pentagons and heptagons; a semiconducting planar sheet formed by four- and eight-atom carbon rings [6]; and even a buckled 2D material made of distorted pentagons, known as pentagraphene [7,8]. The two latter examples attract interest for being semiconductor planar forms of carbon which could complement graphene. Additionally, structures combining hexagonal and other *n*-carbon rings have been proposed [9,10]. Among them, biphenylene stands out due to its recent experimental synthesis via the dehydrofluorination fusion of benzenoid polyphenylene chains [11]. This planar *sp*² carbon network structure was proposed long ago [12]. It exhibits an intricate geometry, comprising four-, six- and eight-fold rings. The electronic stability of biphenylene systems was also studied before its synthesis by means of first-principles calculations, including ribbons and tubes of different widths and morphologies [13].

After its experimental discovery, many works have explored the physical and chemical properties of biphenylene [14–18]. Density functional theory (DFT) calculations identified a type-II Dirac cone with metallic character which could be useful for valleytronics due to the existence of two bands with the same sign of the carrier velocity [19–21]. However, a band gap can be achieved by applying strain or doping the lattice [22,23]. Another way of producing a band gap is by doping with fluorine atoms; this technique can also be applied to tune the Dirac cone and change its character [24]. Theoretical results predict semiconductor behavior for armchair nanoribbons for small sizes (<2 nm) and metallic behavior for both zigzag and larger armchair ribbons [11,13]. Regarding bilayer systems, the AA stacking was modeled within a DFT approach, predicting a stable configuration with enhanced elastic characteristics compared to its monolayer counterpart [25]. Further studies revealed that biphenylene may have properties of practical interest, such as being an anticorrosion coating material with exceptional oxygen atom adsorption and reasonable hydrophobicity [15] and thermoelectric applications in the 2D system [26] and in nanoribbons [27,28]. With biphenylene nanoribbons as the building block, a new porous three-dimensional metallic carbon structure was also reported [29]. More recently, the topological properties of biphenylene were studied by means of a simple tight-binding model, which allowed the verification of topological phase transitions and exploration of the higher-order topological properties of this material [30].

Motivated by these works, we propose two symmetric bilayer configurations, obtained by lattice displacements of one of the layers and with minimal translational unit cells. We denominate these bilayer stackings AB, in analogy with bilayer

*Current address: Nanotechnology Group, USAL – Nanolab, University of Salamanca, 37008, Salamanca, Spain.

graphene, and AX, which is found by displacing one layer along the x direction starting from the direct stacking AA. Importantly, the relaxed DFT calculations of the proposed bilayer structures yield a similar total energy. Our main findings are the following: (1) We propose two symmetric stackings for bilayer biphenylene, AB and AX, with comparable total energies with respect to the AA case, which indicates their experimental feasibility. (2) A type-II Dirac cone is reproduced by adopting our tight-binding parametrization. We have verified that the Dirac cone is robust and persists in bilayer biphenylene AA, AB, and AX stackings. (3) In armchair nanoribbons with an odd number of hexagons across their width, the Dirac crossing is preserved; for even widths, a gap opens in the cone. We relate this even-odd effect to the mirror symmetry of the wave function with respect to its longitudinal axis. (4) A different number of in-gap topological edge states for wide armchair nanoribbons are obtained with our model compared to simpler parametrizations, which is related to the inclusion of hopping energies between atoms up to 3 Å apart.

We believe that our proposal of different stackings can stimulate the experimental search for these bilayers and the study of their physical properties. Additionally, we expect that our tight-binding model will be of interest for further explorations of complex biphenylene structures with hybrid geometric structures.

II. SYSTEMS AND METHODS

In order to describe all biphenylene structures, we start by performing a DFT relaxation of the geometries. With the relaxed coordinates, we perform a general tight-binding parametrization intended to be valid for all structures, i.e., applicable to the monolayer and also to nanoribbons and bilayers. Due to the low atomic number of carbon, we do not include spin-orbit coupling (SOC) effects, expecting a very small value, as in graphene [31]. We have verified that the SOC splitting in biphenylene is of the order of meV, so it is also negligible unless one is seeking very low temperature effects.

A. Geometry of monolayer biphenylene

Different from graphene, monolayer biphenylene belongs to the $Pmmm$ space group. It is described by a rectangular unit cell of orthogonal lattice vectors \vec{a}_1 and \vec{a}_2 of unequal lengths $a_1 \neq a_2$ with a six-atom basis, as depicted in Fig. 1(a). Note that the hexagon is not regular, and neighboring atoms are at two different distances, d_1 and d_2 . Repeating this pattern, octagons and four-atom rings are distinguished in Fig. 1(a), so four different distances between atoms are required. The relaxed geometries obtained by DFT for the monolayer are the following: The lengths of the lattice vectors are $a_1 = 3.82$ Å and $a_2 = 4.54$ Å, with octagon angles $\theta_1 = 125^\circ$ and $\theta_2 = 145^\circ$. The four distances between atoms with primary covalent bonds, defined in Fig. 1(a), are given by $d_1 = 1.42$ Å, $d_2 = 1.44$ Å, $d_3 = 1.50$ Å, and $d_4 = 1.47$ Å, as given in Table I. The basis vectors can be written as $\vec{a}_1 = (2d_1 \sin(\pi - \theta_2) + d_3, 0)$ and $\vec{a}_2 = (0, d_1 \cos(\pi - \theta_2) + d_2)$. The first Brillouin zone, also rectangular, is depicted in Fig. 1(a), with the four high-symmetry points labeled, namely, $\Gamma = (0, 0)$, $X = (\frac{\pi}{a_1}, 0)$, $Y = (0, \frac{\pi}{a_2})$, and $S = (\frac{\pi}{a_1}, \frac{\pi}{a_2})$.

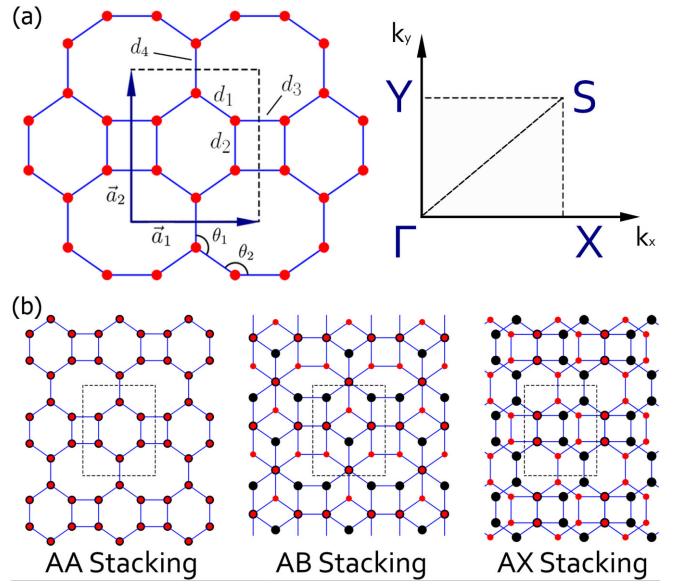


FIG. 1. (a) Left: 2D biphenylene lattice with primitive vectors \vec{a}_1 and \vec{a}_2 along the x and y directions, respectively. Right: first Brillouin zone of biphenylene with special symmetry lines and points. (b) Schematic depiction of the three bilayer stackings studied in this work.

B. Geometries of bilayers with symmetric stackings

The geometric stackings for bilayer biphenylene defined as AA, AB, and AX are depicted in Fig. 1(b), belonging to space groups $Pmmm$ in the AA case and $P2/m$ for AB and AX. Bilayer AA is the trivial, direct stacking, obtained by placing two biphenylene layers one on top of the other, studied in a previous work [25]; we also model this bilayer for completeness. We obtain the AB stacking from an AA bilayer, displacing one of the layers a distance d_2 along the \vec{a}_2 direction [see middle panel of Fig. 1(b)]. We choose this denomination (AB) because one atom belonging to a hexagon of the upper layer is in the center of the hexagon of the bottom layer, thus resembling the AB stacking of bilayer graphene. Finally, we derive the AX bilayer by starting from the AA configuration and displacing one layer by a distance d_3 along the \vec{a}_1 direction; it resembles the so-called slip stacking visible in graphene moiré patterns, as can be seen in the right panel of Fig. 1(b) [32,33].

The proposed stackings AB and AX have total energies similar to that of the reportedly stable AA stacking within our DFT calculations, as detailed in Table II. In fact, they are so close that it may be possible to change stacking by sliding one layer on top of the other. In all these cases the unit cell has

TABLE I. Lattice parameters for the monolayer and bilayer obtained from DFT (GGA-PBE) relaxation and fitted parameters for the TB calculations.

Lattice parameters	2D TB parameters
$d_1 = 1.42$ Å	$t_1 = -3.3$ eV
$d_2 = 1.44$ Å	$t_0 = -0.33$ eV
$d_3 = 1.50$ Å	$\alpha = 1.45$
$d_4 = 1.47$ Å	$\beta = 2.2$

TABLE II. Energy differences ΔE relative to AA stacking (in meV/atom) obtained from DFT relaxed structures within the GGA-PBE, vdW-DF, and vdW-DF2-equivalent functionals.

Functional	ΔE (AB-AA)	ΔE (AX-AA)
GGA-PBE	1.031	0.846
vdW-DF	0.453	0.105
vdW-DF2	0.038	-0.422

12 atoms, 2 times more than that of the monolayer; the ideal (unrelaxed) lattice vectors are initially chosen to be the same as for the monolayer and change after relaxation, as expected. The interlayer distance is close to that of graphene, and we obtained slightly different values after relaxation, which will be discussed later. The interlayer distances also depend on the functional employed, see Supplemental Material Ref. [34].

C. DFT calculations

The SIESTA first-principles code [35,36] is employed to perform electronic structure calculations, using the generalized gradient approximation (GGA) and the Perdew-Burke-Ernzerhof (PBE) exchange-correlation functional [37]. This is our functional of choice for the monolayer system. For the bilayer geometries, additional van der Waals density functionals (vdw-DF) following Dion *et al.* [38] with different improvements were used. Namely, the Dion-Rydberg-Schröder-Langreth-Lundqvist (DRSLL), equivalent to vdW-DF [39] and Lee-Murray-Kong-Lundqvist-Langreth (LMKLL), equivalent to vdW-DF2 [40] flavors. For all calculations, a double- ζ singly polarized basis set was employed. The reciprocal space was mapped by means of an $8 \times 8 \times 1$ Monkhorst-Pack grid for all systems. All structures were relaxed until the forces were below 0.01 eV/\AA . We do not include SOC effects in the reported results, although we verified that they are negligible (1–2 meV) for practical purposes, unless very low temperatures (below liquid nitrogen) are considered.

D. Tight-binding approach

Our goal with the tight-binding approach is to provide a unified description of all biphenylene structures. Since we focus on the bands around the Fermi energy, a single p_z orbital tight-binding (TB) Hamiltonian is used to describe the bilayer and monolayer systems, given by

$$H = \sum_{i,a} \varepsilon_i^a c_i^{\dagger a} c_i^a + \sum_{i,j,a} t_{ij}^a c_i^{\dagger a} c_j^a + \sum_{i,j,a,b} t_{ij}^{\perp ab} c_i^{\dagger a} c_j^b + \text{H.c.}, \quad (1)$$

where ε_i^a is the on-site energy for each atom located at site i in layer a and the operator $c_i^{\dagger a}$ (c_i^a) creates (annihilates) an electron on site i in layer a . The second term describes the intralayer couplings, with t_{ij}^a being the corresponding hopping energies within layer a . Obviously, for monolayers $a = 1$, and the third summation is omitted; for bilayers we consider two values, a (b) = 1, 2, as well as the interlayer interactions, given by the last term ($a \neq b$) and denoted as $t_{ij}^{\perp ab}$. They depend on the stacking configuration between the top and bottom biphenylene layers.

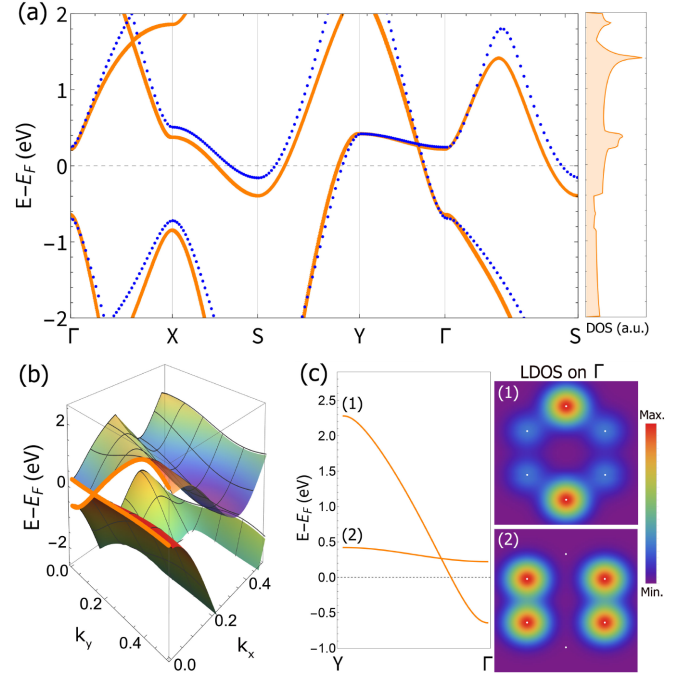


FIG. 2. (a) Biphenylene electronic structure: DFT (blue dotted curves) and TB (orange bands) results with on-site energies $\varepsilon_1 = -2.2 \text{ eV}$ and $\varepsilon_2 = -1.85 \text{ eV}$ for sites (1) and (2) in (c), respectively, $t_1 = -3.3 \text{ eV}$, and $\beta = 2.2$. The DOS for the TB bands is shown on the right. (b) Two-dimensional TB energy bands highlighting the type-II Dirac cone (orange). (c) Zoom along the Y - Γ line focusing on the type-II Dirac cone, with LDOS for the two bands on the right. Atomic positions in the unit cell are marked with white dots; red and purple indicate maximum and minimum probability densities.

To find a suitable hopping parametrization we consider an intralayer hopping energy described by a decaying exponential function [33],

$$t_{ij}^a = t_1 e^{-\beta \left(\frac{r_{ij}}{d_1} - 1 \right)}, \quad (2)$$

with r_{ij} being the distance between the i and j lattice sites, t_1 being the hopping related to the first-nearest-neighbor distance d_1 , and β being a fitting parameter that controls the range of the interaction. As the ratio r_{ij}/d_1 is always larger than 1 beyond the first nearest neighbors, small β values allow us to increase the number of neighbors with non-negligible hoppings in the description.

For the interlayer connection we also consider a decaying exponential function for the hopping energies given by

$$t_{ij}^{\perp ab} = t_0 e^{-\alpha \left(\frac{r_{ij}}{d_{\perp}} - 1 \right)}, \quad (3)$$

where d_{\perp} is the interlayer distance; t_0 is the direct stacking hopping value, i.e., when the atoms are exactly one above the other; and α modulates the strength of the interlayer hopping with increasing distance.

III. TWO-DIMENSIONAL BIPHENYLENE SYSTEMS

A. Monolayer biphenylene

We present in Fig. 2(a) a comparison between DFT GGA-PBE (dotted blue curves) and the fitted tight-binding (solid

orange lines) band calculations. The agreement is very good for the fitting parameters shown in Table I, especially in the energy range close to the Fermi level. The density of states (DOS) obtained from the TB approach is displayed to the right of the electronic bands. The peculiar type-II Dirac cone appearing in the middle of the Y - Γ path can be clearly seen in Fig. 2(a), and it is correctly described by the TB model by adjusting the in-plane parameter β . A 2D plot of the band structure is depicted in Fig. 2(b), where the type-II cone is highlighted in orange.

A zoom of the bands along Y - Γ constituting the type-II Dirac cone, labeled 1 and 2, is presented in Fig. 2(c). The local density of states (LDOS) of the respective bands, calculated at the Γ point, is depicted to the right of the electronic bands. Note that the LDOSs of the two bands are localized in different regions of the unit cell, having maxima at different atoms. The two atoms with maximum LDOS in the top right panel of Fig. 2(c), corresponding to band 1, are related by a mirror symmetry of the system. Likewise, the four atoms with maximum LDOS in the bottom right panel, corresponding to band 2, are also related by mirror symmetries of the 2D crystal. However, there is no symmetry operation that relates these two sets of atoms [41]. Therefore, these states do not interact, and the bands cross, as seen in the left panel of Fig. 2(c). At the crossing energy (not shown here), all sites have a nonzero density. Since these two sets of atoms are not related by symmetry, a small variation in their respective on-site energies can be included to fit with our DFT results: $\varepsilon_1 = -2.2$ eV and $\varepsilon_2 = -1.85$ eV for the respective sets.

We also corroborate that there is a crossing at the Dirac cone by checking that the bands constituting this cone along the symmetry line connecting the Y and Γ points belong to different irreducible representations [42,43] when no SOC is included, as previously reported [30]. We should mention, however, that if SOC is included, these bands belong to the same irreducible representation and present a very small anti-crossing due to the weak SOC in biphenylene.

It is important to emphasize that the use of a tight-binding parametrization with an exponential decay which includes hoppings between atoms up to 3 Å is crucial in our model to obtain the predicted type-II Dirac cone in biphenylene and similar materials, in agreement with DFT calculations. The overall picture of the hopping decay parametrization with the neighbor distances is shown in Fig. 3, with the hopping scheme given in the inset, where each group of neighbors is highlighted by colored regions labeled I, II, and III. Region I corresponds to hoppings between atoms with primary bonds (black solid lines), region II is for intermediate distances (colored solid lines), and region III corresponds to long-range hoppings (colored dashed lines). The slope of the bands is determined by the β parameter, and altering it affects carrier velocities. This adjustment can be tuned to achieve the desired characteristics of the bands. Additionally, it is essential to take into account a sufficient number of neighbors. To achieve the desired type-II Dirac cone we must include hoppings up to region III, which is equivalent to considering distances greater than those marked by the green dashed lines (>3 Å) in the schematic inset. Not considering enough hopping parameters results in a completely flat energy band along the Y - Γ direction in one of the branches of the Dirac cone, changing

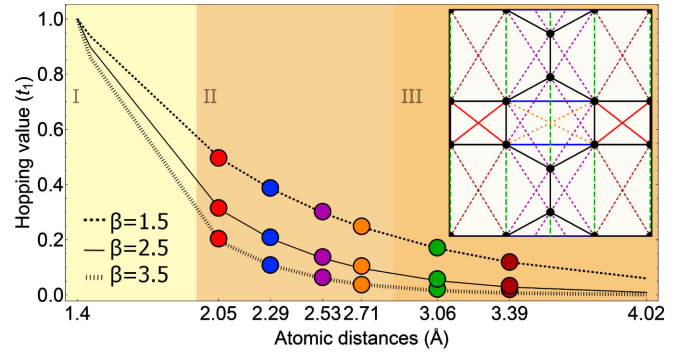


FIG. 3. Illustration of in-plane hopping energies as a function of the atomic lattice distances for different values of the decay parameter β . Colored circles illustrate hoppings at different lattice distances, matching the color code employed in the schematic lattice geometry shown in the inset. The distances and hoppings are grouped by shaded regions, labeled I, II, and III.

its character to type III [24,30]. Therefore, a careful choice of both the β parameter and hence the range of neighbors included is critical to obtain the desired band features. We believe that this parametrization approach will also be helpful in other systems in which intricate symmetries and numerous hopping distances may hinder the derivation of optimal physical parameters for theories based on a TB model theory of the structure.

B. Bilayer biphenylene: AA, AB, and AX stackings

For bilayer biphenylene systems, we include the van der Waals interaction in the DFT calculations by means of a vdW-DF2-equivalent functional. As in the case of the monolayer, the lattice parameters included in TB calculations were obtained from previous DFT relaxations. We find that the intralayer and the internal angles are the same as for the monolayer.

Table II displays the energy difference ΔE (meV/atom) between stackings AB and AX relative to AA. We take the AA bilayer as a reference because its stability was previously established [25]. Besides the fact that for vdW-DF2 this energy difference is negative for AX, the AA stacking has the smallest energy for GGA-PBE and vdW-DF functionals; remarkably, we have found that AX is more stable if the DF2-equivalent functional is employed. Since the energy differences in biphenylene bilayers are close to meV, our results point to the experimental feasibility of all these stackings and the possibility to change from one to another.

The unit vectors in the bilayer predicted by DFT are $a_1 = 3.84$ Å and $a_2 = 4.54$ Å. Previous DFT calculations [25] predicted a biphenylene interlayer distance of 3.36 Å in the AA stacking, a value notably close to that of bilayer graphene (3.42 Å). However, our calculations yield a larger distance for the AA stacking. The values for the three studied stackings reveal a small variation for the interlayer distances. In our calculation, the AB stacking has the smallest interlayer spacing. The smallest interlayer distances for the AA, AB, and AX stackings correspond to the vdW-DF2-equivalent functional and are 3.51, 3.39, and 3.43 Å, respectively. In the Supplemental Material [34] we show a comparison of the

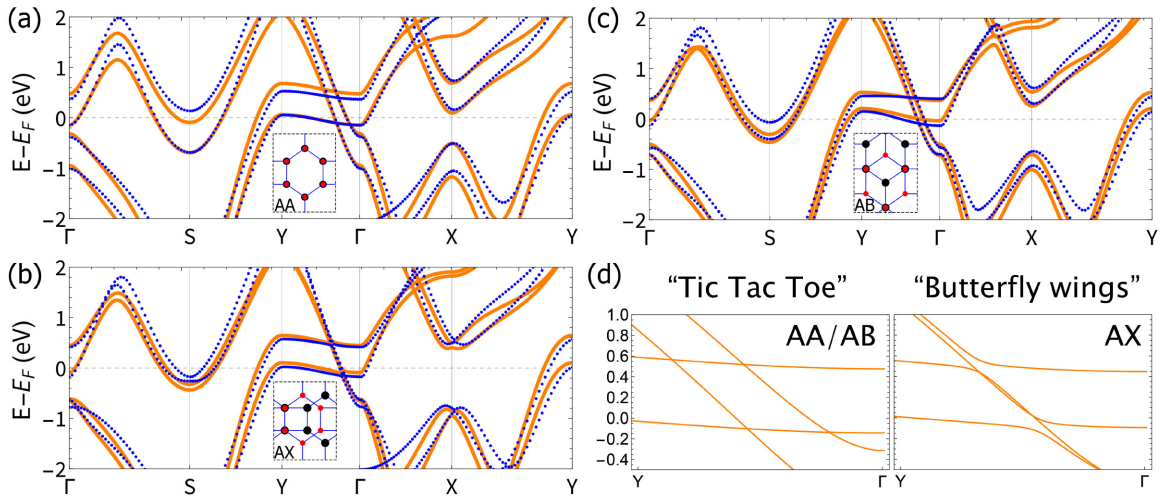


FIG. 4. Bilayer biphenylene band structures for the three stackings considered: (a) AA, (b) AB, and (c) AX stackings. The corresponding unit cells are shown in the insets, marked with dashed lines. DFT bands are shown by blue dots, and TB are shown by orange curves; the parameters chosen are $\alpha = 1.45$, $\beta = 2.2$, $t_0 = -0.33$ eV, $t_1 = -3.3$ eV, $\varepsilon_1 = -2.2$ eV, and $\varepsilon_2 = -1.85$ eV. (d) Zooms of the bands at the split Dirac point showing the crossing/anticrossing behavior. Left panel full crossings characteristic of the AA/AB geometries, labeled tic-tac-toe. Right panel partial anticrossing corresponding to the AX stacking, named butterfly wings.

energy bands computed using different DFT functionals, in particular, GGA-PBE, vdW-DF, and vdW-DF2 equivalents. The TB parameters used are $\alpha = 1.45$ and $t_0 = -0.33$ eV for the interlayer coupling; the same intralayer parameters used in the case of the monolayer are adopted.

In Figs. 4(a)–4(c) we compare the DFT and TB band structures of the three stacking configurations, AA, AX, and AB, respectively. We verify that the agreement between the TB and DFT bands is very satisfactory. Notice that, due to interlayer coupling, the type-II Dirac cones are doubled, as expected. Moreover, one of the cones crosses the Fermi energy for the three proposed stackings. This is an important feature for transport applications. Notice that the split bands forming the Dirac cones are more separated in the AA case, whereas for AB and AX there is clear asymmetry in the splittings: The flat bands are rather separated, but the bands with a larger slope are much closer in energy. An energy zoom allows us to distinguish two types of crossings, as depicted in Fig. 4(d). Notice that the bands have either a tic-tac-toe shape, with four Dirac points, like for AA and AB stackings, or a partial anticrossing, with only two bands crossings, like for AX. We denote the latter band crossing shape as “butterfly wings.”

IV. ARMCHAIR NANORIBBONS

In what follows, we perform biphenylene nanoribbon (NR) calculations to verify the effectiveness and convenience of the proposed TB parametrization in such quasi-one-dimensional (quasi-1D) systems. The atomic coordinates are obtained from the relaxed DFT (GGA-PBE) calculations of the monolayer without performing further relaxations to take into account edge effects. We verified by comparison to other DFT calculations [11] that the edge effects are not important in such nanoribbons; in fact, our results are quite similar to the relaxed ones reported therein. We focus on the armchair edges, which are known to have a semiconductor nature for smaller widths. We denote the ribbons by n -NR, where n denotes the width

of the ribbon given in dimer chains, as it can be seen in the right panels of Fig. 5 for two cases, 18-NR and 25-NR. To facilitate the comparison to the 2D case, we label the first Brillouin zone of these ribbons using the same label, Γ - Y . The optimal parametrization has the same in-plane hopping, $t_1 = 3.3$ eV, as that used for the 2D system and an adjusted on-site energy ε and exponential parameter β , $\varepsilon = -1.3$ eV and $\beta = 2.6$, respectively. Note that the nanoribbon bands computed with this parametrization are in good agreement with the relaxed DFT nanoribbons calculated by Fan *et al.* [11]. This indicates that edge effects are not important for small widths, so it is not necessary to include them in the

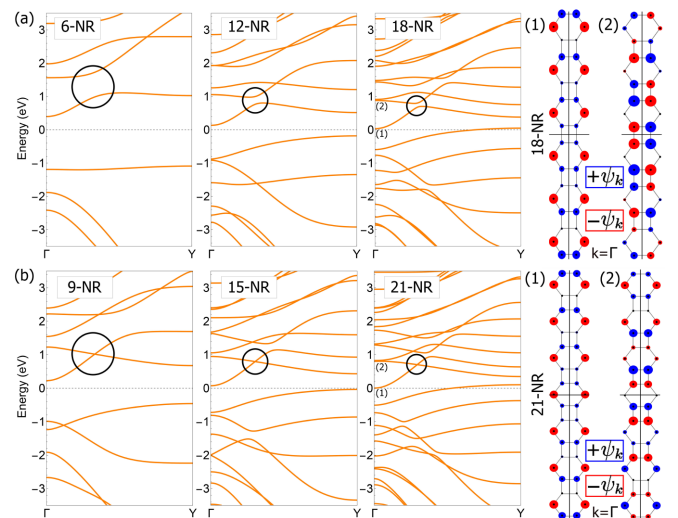


FIG. 5. Electronic band structures of armchair nanoribbons with (a) even (6-NR, 12-NR, and 18-NR) and (b) odd (9-NR, 15-NR, and 21-NR) widths. Wave function $\psi_{k=\Gamma}$ values and signs for the 18-NR and 21-NR are represented by the sizes and colors of circles within the unit cell, respectively, for bands 1 and 2. The TB parameters are $t_1 = -3.3$ eV, $\beta = 2.6$, and $\varepsilon = -1.3$ eV.

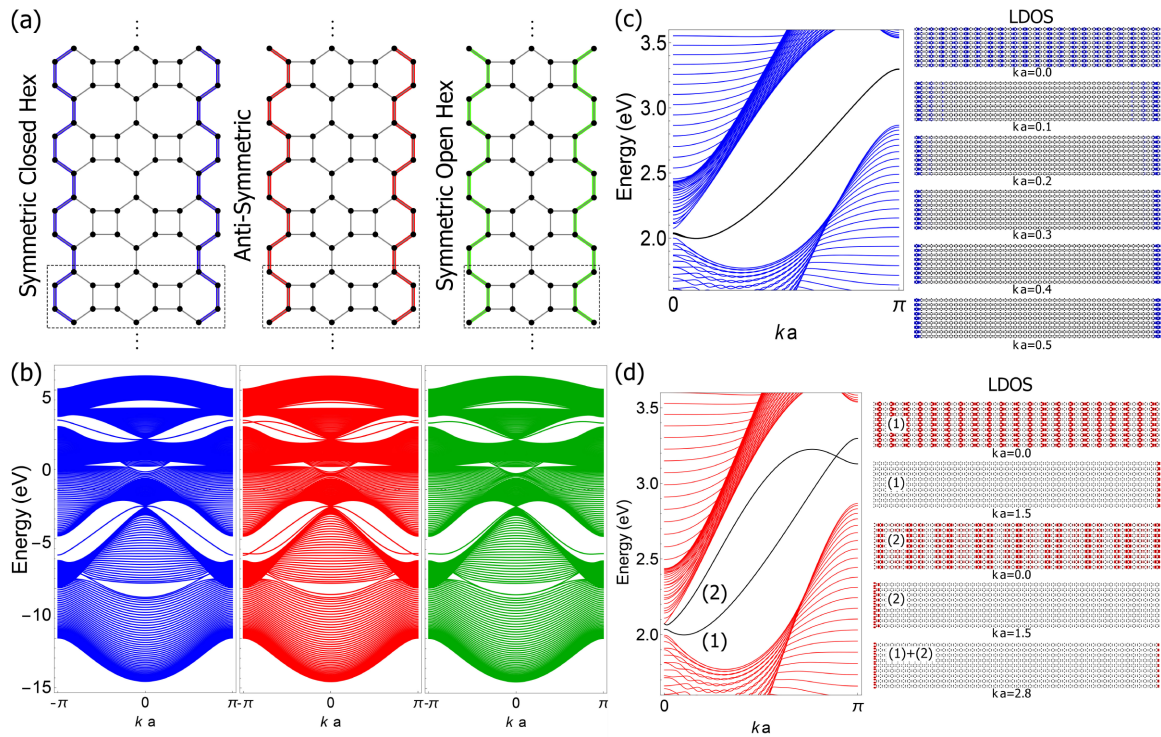


FIG. 6. (a) The 9-NR armchair nanoribbon geometries for three edge configurations: symmetric closed hexagons (SCHs), antisymmetric (AS), and symmetric open hexagons (SOHs), shown in blue, red, and green, respectively. (b) Electronic bands of 50-NRs for the three edge configurations ($\beta = 2.6$ and $\varepsilon = 0$). Zoom of the electronic bands of the (c) SCH and (d) AS 50-NRs and projected LDOS for different ka values over the nanoribbon sites highlighted in black in (a). Parameters are $t_1 = -3.3$ eV, $\beta = 2.6$, and $\varepsilon = -1.3$ eV.

tight-binding nanoribbon calculations, especially for large widths.

A type-II Dirac cone is also observed for nanoribbons with an odd number of hexagons across their width. However, for those with an even width, a gap opens, destroying the cone. This behavior is highlighted in Figs. 5(a) and 5(b) by black circles at the anticrossing or crossing regions for even and odd ribbons, respectively. The projected wave functions inside the unit cells at the Γ point for the 18-NR and 21-NR are depicted on the right side of the respective band structures in Fig. 5. The sign of the wave function is represented by the different colors, and the amplitude is indicated by the disk size. Notice that the wave functions of the low-lying band at Γ , labeled 1, presents two mirror symmetries with respect to the horizontal (M_h) and vertical (M_v) planes marked with black lines, as well as inversion symmetry I . However, the wave function of the upper band, labeled 2, has fewer different symmetries, which vary with the nanoribbon width. In the case shown in Fig. 5(a), the 18-NR, it is M_h ; for Fig. 5(b), corresponding to 21-NR, it is M_v . The horizontal mirror symmetry is important for the confined wave functions; note that the probability density is symmetric with respect to the longitudinal axes of the ribbons. Therefore, if the wave functions of bands 1 and 2 share this symmetry (for even widths), their bands anticross, whereas for odd ribbons, for which these bands do not share this reflection symmetry, the bands cross and the Dirac cone is preserved. This even-odd behavior is identical to the parity change of wave functions for successive states in textbook quantum wells with respect to their centers. Here, the

wave functions change differently with respect to the different mirror reflections; however, the important mirror symmetry for this even-odd behavior is the reflection with respect to the longitudinal axes. Similar symmetry arguments have successfully explained even-odd effects in other graphene-based nanoribbons [44] and slabs of topological materials [45,46]. The same parametrization was also employed for the study of wide ribbons.

In Fig. 6(a) we present three edge configurations in the armchair features: symmetric closed hexagons (SCHs), antisymmetric (AS), and symmetric open hexagons (SOHs), represented by blue, red, and green edges, respectively. Using the same color scheme, the electronic bands for each edge configuration are shown at Fig. 6(b) with parameters $t_1 = -3.3$ eV, $\beta = 2.6$, and $\varepsilon = -1.3$ eV. The energy states are, on average, the same for the three geometries considered. However, distinguishable isolated states located between the bulk energy bands, within the pseudogaps, are found for each of the three edge symmetries.

A zoom of the twofold degenerate SCH band structure (blue curves) is shown in Fig. 6(c). The LDOS is computed for this specific state between $ka = 0$ and $ka = 0.5$. At $ka = 0$, we note that the charge density is spread over all the nanoribbon because at this point the edge bands meet the bulk bands. A change in the charge distribution happens, however, as shown for $ka = 0.1$ up to $ka = 0.5$, at the Brillouin zone boundary. Highly localized states emerge at the nanoribbon edges for $ka \neq 0$. Compared with the other symmetric edge nanoribbon SOH, such in-gap edge states emerging in the

electronic bands are also degenerate like for the SCH case. With respect to the AS nanoribbon, the twofold degeneracy is broken in such localized states, resulting in complementary edge states for bands 1 and 2, respectively, at $ka = 1.5$, as shown in the LDOS of Fig. 6(d). At the band crossing ($ka = 2.8$), the charge densities are localized at both edges, as seen in the 1+2 LDOS case. Recently, a two-hopping tight-binding parametrization found via Zak phase calculations that such edge states are topological [30]. Actually, by employing our exponential hopping parametrization we have verified that those edge states may change in number and energy, suggesting different Zak phases in the involved cases.

V. CONCLUSIONS

We introduced two biphenylene bilayer stackings, AB and AX. The bands are split due to the interlayer interaction, and one of the type-II Dirac cones is placed at the Fermi energy, suggesting different transport responses. The AB and AX stackings present total energies similar to that of AA bilayer biphenylene, which is reported to be stable. This indicates that AB and AX stackings might be experimentally achievable as well.

We derived a robust tight-binding parametrization based on DFT calculations to describe the electronic structure of various biphenylene systems, including monolayers, bilayers, and nanoribbons of different widths. We confirmed the presence of a type-II Dirac cone in both monolayer and bilayer geometries, in agreement with previous works. By means of DFT calculations, we obtained relaxed structures that allowed us to fit our TB model, successfully capturing the electronic properties of biphenylene-based structures. The TB parametrization

preserves essential symmetries and ensures the type-II nature of the Dirac cone by extending hopping up to third-neighbor group distances ($>3 \text{ \AA}$).

Our combined approach correctly describes the type-II Dirac cone in both 2D and quasi-1D biphenylene structures, revealing crossings and anticrossings in the Dirac cone for nanoribbons depending on their width due to the different symmetries in their corresponding wave functions. Additionally, for wider nanoribbons, our calculations allow the identification of robust edge states localized at the edges of the unit cell. We expect that our findings will motivate further theoretical and experimental work. Moreover, the present study is also applicable to other carbon-based systems with hybrid geometric symmetries, like pentacomposites and other allotropes such graphenylene.

ACKNOWLEDGMENTS

The authors would like to thank INCT de Nanomateriais de Carbono for providing support on the computational infrastructure. L.L.L. acknowledges a CNPq scholarship. A.L. thanks the CNPq and FAPERJ for Grants No. E-26/202.567/2019 and No. E-26/200.569/2023. L.C. and O.A.-G. acknowledge financial support from the Agencia Estatal de Investigación under Grant No. PID2022-136285NB-C31 and from Grant No. (MAD2D-CM)–(UCM5), Recovery, Transformation and Resilience Plan, funded by the Comunidad de Madrid, European Union, NextGenerationEU. O.A.-G. acknowledges the support of Grant No. PRE2019-088874 funded by MCIN/AEI/10.13039/501100011033 and by “ESF Investing in your future.” J. D. Correa and S. Bravo are gratefully acknowledged for illuminating conversations.

-
- [1] J. Li and Y. Han, Artificial carbon allotrope gamma-graphyne: Synthesis, properties, and applications, *Giant* **13**, 100140 (2023).
- [2] D. C. M. Rodrigues, L. L. Lage, P. Venezuela, and A. Latgé, Exploring the enhancement of the thermoelectric properties of bilayer graphyne nanoribbons, *Phys. Chem. Chem. Phys.* **24**, 9324 (2022).
- [3] D. C. M. Rodrigues, R. G. Amorim, A. Latgé, and P. Venezuela, Improving the sensitivity of graphyne nanosensor by transition metal doping, *Carbon* **212**, 118087 (2023).
- [4] X. Zheng, S. Chen, J. Li, H. Wu, C. Zhang, D. Zhang, X. Chen, Y. Gao, F. He, L. Hui, H. Liu, T. Jiu, N. Wang, G. Li, J. Xu, Y. Xue, C. Huang, C. Chen, Y. Guo, T.-B. Lu, Two-dimensional carbon graphdiyne: Advances in fundamental and application research, *ACS Nano* **17**, 14309 (2023).
- [5] V. H. Crespi, L. X. Benedict, M. L. Cohen, and S. G. Louie, Prediction of a pure-carbon planar covalent metal, *Phys. Rev. B* **53**, R13303 (1996).
- [6] J. Nisar, X. Jiang, B. Pathak, J. Zhao, T. W. Kang, and R. Ahuja, Semiconducting allotrope of graphene, *Nanotechnology* **23**, 385704 (2012).
- [7] C.-P. Tang, S.-J. Xiong, W.-J. Shi, and J. Cao, Two-dimensional pentagonal crystals and possible spin-polarized dirac dispersion relations, *J. Appl. Phys.* **115**, 113702 (2014).
- [8] S. Zhang, J. Zhou, Q. Wang, X. Chen, Y. Kawazoe, and P. Jena, Penta-graphene: A new carbon allotrope, *Proc. Natl. Acad. Sci. USA* **112**, 2372 (2015).
- [9] L.-C. Xu, R.-Z. Wang, M.-S. Miao, X.-L. Wei, Y.-P. Chen, H. Yan, W.-M. Lau, L.-M. Liu, and Y.-M. Ma, Two dimensional Dirac carbon allotropes from graphene, *Nanoscale* **6**, 1113 (2014).
- [10] A. Bandyopadhyay, S. Datta, D. Jana, S. Nath, and M. M. Uddin, The topology and robustness of two Dirac cones in S-graphene: A tight binding approach, *Sci. Rep.* **10**, 2502 (2020).
- [11] Q. Fan, L. Yan, M. Tripp, O. Krejčí, S. Dimosthenous, S. Kachel, M. Chen, A. Foster, U. Koert, P. Liljeroth, and J. Gottfried, Biphenylene network: A nonbenzenoid carbon allotrope, *Science* **372**, 852 (2021).
- [12] A. T. Balaban, C. C. Rentia, and E. Ciupitu, Estimation of the relative stability of several planar and tridimensional lattices for elementary carbon, *Rev. Roum. Chim.* **13**, 231 (1968).
- [13] M. A. Hudspeth, B. W. Whitman, V. Barone, and J. E. Peralta, Electronic properties of the biphenylene sheet and its one-dimensional derivatives, *ACS Nano* **4**, 4565 (2010).
- [14] Y. Luo, C. Ren, Y. Xu, J. Yu, S. Wang, and M. Sun, A first principles investigation on the structural, mechanical, electronic, and catalytic properties of biphenylene, *Sci. Rep.* **11**, 98589 (2021).

- [15] K. Ke, K. Meng, J. Rong, and X. Yu, Biphenylene: A two-dimensional graphene-based coating with superior anti-corrosion performance, *Materials* **15**, 5675 (2022).
- [16] S. Demirci, T. Gorkan, S. Çalloğlu, V. O. Özçelik, J. V. Barth, E. Aktürk, and S. Çiraci, Hydrogenated carbon monolayer in biphenylene network offers a potential paradigm for nanoelectronic devices, *J. Phys. Chem. C* **126**, 15491 (2022).
- [17] Y.-W. Son, H. Jin, and S. Kim, Magnetic ordering, anomalous Lifshitz transition, and topological grain boundaries in two-dimensional biphenylene network, *Nano Lett.* **22**, 3112 (2022).
- [18] K. Niu, Q. Fan, L. Chi, J. Rosen, J. M. Gottfried, and J. Björk, Unveiling the formation mechanism of the biphenylene network, *Nanoscale Horiz.* **8**, 368 (2023).
- [19] P.-F. Liu, J. Li, C. Zhang, X. H. Tu, J. Zhang, P. Zhang, B.-T. Wang, and D. J. Singh, Type-II Dirac cones and electron-phonon interaction in monolayer biphenylene from first-principles calculations, *Phys. Rev. B* **104**, 235422 (2021).
- [20] I. Alcón, G. Calogero, N. Papior, A. Antidormi, K. Song, A. W. Cummings, M. Brandbyge, and S. Roche, Unveiling the multi-radical character of the biphenylene network and its anisotropic charge transport, *J. Am. Chem. Soc.* **144**, 8278 (2022).
- [21] A. Bafekry, M. Faraji, M. M. Fadlallah, H. R. Jappor, S. Karbasizadeh, M. Ghergherehchi, and D. Gogova, Biphenylene monolayer as a two-dimensional nonbenzenoid carbon allotrope: A first-principles study, *J. Phys.: Condens. Matter* **34**, 015001 (2022).
- [22] Y. Hou, K. Ren, Y. Wei, D. Yang, Z. Cui, and K. Wang, Opening a band gap in biphenylene monolayer via strain: A first-principles study, *Molecules* **28**, 4178 (2023).
- [23] S. Lee, A. Singh, and H. Lee, Band gap engineering of 2D biphenylene carbon sheets with hydrogenation, *J. Korean Phys. Soc.* **79**, 846 (2021).
- [24] S. Mo, J. Seo, S.-K. Son, S. Kim, J.-W. Rhim, and H. Lee, Engineering two-dimensional nodal semimetals in functionalized biphenylene by fluorine adatoms, *Nano. Letters* **24**, 4885 (2024).
- [25] S. Chowdhury, S. Ghosal, D. Mondal, and D. Jana, First-principles and machine-learning study of electronic and phonon transport in carbon-based AA-stacked bilayer biphenylene nanosheets, *J. Phys. Chem. Solids* **170**, 110909 (2022).
- [26] A. Kumar, P. Senapati, and P. Parida, Theoretical insights into the structural, electronic and thermoelectric properties of the inorganic biphenylene monolayer, *Phys. Chem. Chem. Phys.* **26**, 2044 (2024).
- [27] Z.-X. Xie, X.-K. Chen, X. Yu, Y.-X. Deng, Y. Zhang, W.-X. Zhou, and P.-Z. Jia, Intrinsic thermoelectric properties in biphenylene nanoribbons and effect of lattice defects, *Comput. Mater. Sci.* **220**, 112041 (2023).
- [28] O. Farzadian, M. Zarghami Dehaghani, K. V. Kostas, A. H. Mashhadzadeh, and C. Spitas, A theoretical insight into phonon heat transport in graphene/biphenylene superlattice nanoribbons: A molecular dynamic study, *Nanotechnology* **33**, 355705 (2022).
- [29] W. Sun, Y. Shen, D. Nia, and Q. Wang, A biphenylene nanoribbon-based 3D metallic and ductile carbon allotrope, *Nanoscale* **14**, 3801 (2022).
- [30] K. Koizumi, H. T. Phan, K. Nishigomi, and K. Wakabayashi, Topological edge and corner states in the biphenylene network, *Phys. Rev. B* **109**, 035431 (2024).
- [31] S. Kunschuh, M. Gmitra, and J. Fabian, Tight-binding theory of the spin-orbit coupling in graphene, *Phys. Rev. B* **82**, 245412 (2010).
- [32] G. Li, A. Luican, J. M. B. Lopes dos Santos, A. H. Castro Neto, A. Reina, J. Kong, and E. Y. Andrei, Observation of Van Hove singularities in twisted graphene layers, *Nat. Phys.* **6**, 109 (2010).
- [33] E. Suarez Morell, P. Vargas, L. Chico, and L. Brey, Charge redistribution and interlayer coupling in twisted bilayer graphene under electric fields, *Phys. Rev. B* **84**, 195421 (2011).
- [34] See Supplemental Material at <http://link.aps.org/supplemental/10.1103/PhysRevB.110.165423> for relaxed coordinates, interlayer distances and band structures obtained with different functionals.
- [35] J. M. Soler, E. Artacho, J. D. Gale, A. García, J. Junquera, P. Ordejón, and D. Sánchez-Portal, The SIESTA method for *ab initio* order-*N* materials simulation, *J. Phys.: Condens. Matter* **14**, 2745 (2002).
- [36] A. García, N. Papior, A. Akhtar, E. Artacho, V. Blum, E. Bosoni, P. Brandimarte, M. Brandbyge, J. I. Cerdá, F. Corsetti, R. Cuadrado, V. Dikan, J. Ferrer, J. Gale, P. García-Fernández, V. M. García-Suárez, S. García, G. Huhs, S. Illera, R. Korytár *et al.*, Siesta: Recent developments and applications, *J. Chem. Phys.* **152**, 204108 (2020).
- [37] J. P. Perdew, K. Burke, and M. Ernzerhof, Generalized gradient approximation made simple, *Phys. Rev. Lett.* **77**, 3865 (1996).
- [38] M. Dion, H. Rydberg, E. Schröder, D. C. Langreth, and B. I. Lundqvist, Van der Waals density functional for general geometries, *Phys. Rev. Lett.* **92**, 246401 (2004).
- [39] G. Román-Pérez and J. M. Soler, Efficient implementation of a van der Waals density functional: Application to double-wall carbon nanotubes, *Phys. Rev. Lett.* **103**, 096102 (2009).
- [40] K. Lee, E. D. Murray, L. Kong, B. I. Lundqvist, and D. C. Langreth, Higher-accuracy van der Waals density functional, *Phys. Rev. B* **82**, 081101(R) (2010).
- [41] D. P. Kuritza, R. H. Miwa, and J. E. Padilha, Directional dependence of the electronic and transport properties of biphenylene under strain conditions, *Phys. Chem. Chem. Phys.* **26**, 12142 (2024).
- [42] Compatibility relations between representations of the double space groups (DCOMPREL), Bilbao Crystallographic Server, <https://www.cryst.ehu.es/cryst/dcomprel>.
- [43] M. Iraola, J. L. Mañes, B. Bradlyn, M. K. Horton, T. Neupert, M. G. Vergniory, and S. S. Tsirkin, IrRep: Symmetry eigenvalues and irreducible representations of *ab initio* band structures, *Comput. Phys. Commun.* **272**, 108226 (2022).
- [44] K. Čerjvevičs, M. Pizzochero, and O. V. Yazyev, Even-odd conductance effect in graphene nanoribbons induced by edge functionalization with aromatic molecules: Basis for novel chemosensors, *Eur. Phys. J. Plus* **135**, 681 (2020).
- [45] A. L. Araújo, G. J. Ferreira, and T. M. Schmidt, Suppressed topological phase transitions due to nonsymmorphism in SnTe stacking, *Sci. Rep.* **8**, 9452 (2018).
- [46] O. Arroyo-Gascón, Y. Baba, J. I. Cerdá, O. de Abril, R. Martínez, F. Domínguez-Adame, and L. Chico, Persistence of symmetry-protected Dirac points at the surface of the topological crystalline insulator SnTe upon impurity doping, *Nanoscale* **14**, 7151 (2022).